Monte Carlo simulations of dense quantum plasmas

V S Filinov[1]**, M Bonitz**[2]**, V E Fortov**[1]**, W Ebeling**[3]**, H Fehske**[4]**, D Kremp**[5]**,
W D Kraeft**[4]**, V Bezkrovniy**[5] **and P Levashov**[1]

[1] Institute for High Energy Density, Izhorskay 13/19, Moscow 125412, Russia
[2] Universität Kiel, Leibnizstrasse 15, 24098 Kiel, Germany
[3] Humbold Universität Berlin, Invalidenstrasse 110, D-10115 Berlin, Germany
[4] Universität Greifswald, Domstrasse 10a, D-17487, Greifswald, Germany
[5] Universität Rostock, Universitätsplatz 3, D-18051 Rostock, Germany

E-mail: filinov@ok.ru

Abstract

Thermodynamic properties of the equilibrium strongly coupled quantum
plasmas investigated by direct path integral Monte Carlo (DPIMC) simulations
within a wide region of density, temperature and positive to negative particle
mass ratio. Pair distribution functions (PDF), equation of state (EOS), internal
energy and Hugoniot are compared with available theoretical and experimental
results. Possibilities of the phase transition in hydrogen and electron–hole
plasma from neutral particle system to metallic-like state and crystal-like
structures, including antiferromagnetic hole structure in semiconductors at low
temperatures, are discussed.

PACS numbers: 52.27.Gr, 71.35.Ee

(Some figures in this article are in colour only in the electronic version)

1. Introduction

The family of Coulomb systems, which are dominated by Coulomb interaction, has grown
beyond conventional plasmas in space or laboratory for many years. They include electron–
hole plasmas in semiconductors, the electron gas in metals, charged particles confined in
various traps or storage rings, charged complexes or dust particles, small few-particle clusters
in mesoscopic quantum dots and so on. The equilibrium properties of *warm dense matter* at
high pressure are of growing importance in many fields, including shock and laser plasmas,
astrophysics, solids and nuclear matter. Among the phenomena of particular current interest
are the high-pressure compressibility of deuterium, metallization of hydrogen, plasma phase
transition, crystallization of one-component plasma (OCP) and two-component plasma (TCP)

etc, which occur in situations where both *interaction and quantum effects* are relevant and a crossover from a neutral particle system to full ionization takes place. The analytical approaches for treatment of Coulomb systems are mainly applicable at low density and high temperature as they are usually based on different kinds of perturbation theories. Therefore, in treatment of strongly coupled Coulomb systems the DPIMC method is of high value, as it avoids additional approximations although at high computational cost. This method now allows simulations of strongly coupled Coulomb systems in a wide range of densities, temperatures and charged particle mass ratio.

2. The direct path integral Monte Carlo method

The starting point for the description of a two-component (equilibrium) quantum plasma is the partition function given at inverse temperature $\beta = 1/k_B T$ by

$$Z(N_e, N_p, V, \beta) = \frac{1}{N_e! N_p!} \sum_\sigma \int_V \mathrm{d}q \, \rho(q, \sigma; \beta), \tag{1}$$

where $q = \{q_e, q_p\}$ and $\sigma = \{\sigma_e, \sigma_p\}$ denote the spatial coordinates and spin degrees of freedom of N_e electrons and N_p protons (or holes) ($N_e = N_p$), i.e. $q_a = \{q_{1,a}, \ldots, q_{l,a}, \ldots, q_{N_a,a}\}$ and $\sigma_a = \{\sigma_{1,a}, \ldots, \sigma_{l,a}, \ldots, \sigma_{N_a,a}\}$ with $a = e, p$. Of course, in general, the exact density matrix $\rho(q, \sigma; \beta)$ of an interacting quantum many-particle systems is not known but can be constructed using a path integral approach:

$$\sum_\sigma \int_V \mathrm{d}q^{(0)} \, \rho(q^{(0)}, \sigma; \beta) = \int_V \mathrm{d}q^{(0)} \cdots \mathrm{d}q^{(n)} \, \rho^{(1)} \cdot \rho^{(2)} \cdots \rho^{(n)}$$
$$\times \sum_\sigma \sum_{P_e} \sum_{P_p} (-1)^{\kappa_{P_e} + \kappa_{P_p}} \mathcal{S}(\sigma, \hat{P}_e \hat{P}_p \sigma') \hat{P}_e \hat{P}_p \rho^{(n+1)}_{q^{(n+1)} = q^{(0)}, \sigma' = \sigma}, \tag{2}$$

where $\rho^{(i)} \equiv \rho(q^{(i-1)}, q^{(i)}; \Delta\beta) \equiv \langle q^{(i-1)} | e^{-\Delta\beta \hat{H}} | q^{(i)} \rangle$ and $\Delta\beta \equiv \beta/(n+1)$. The Hamiltonian for the electron–proton plasma ($\hat{H} = \hat{K} + \hat{U}$) contains kinetic energy ($\hat{K}$) and Coulomb interaction energy ($\hat{U} = \hat{U}_{pp} + \hat{U}_{ee} + \hat{U}_{ep}$) parts. In (2), the index $i = 1, \ldots, n+1$ labels the high-temperature (($n+1$)$k_B T$) density matrices $\rho^{(i)}$. Accordingly, each plasma particle is represented by ($n+1$) points (beads), i.e. the whole configuration of the particles is represented by a $3(N_e + N_p)(n+1)$-dimensional vector $\tilde{q} \equiv \{q_{1,e}^{(0)}, \ldots, q_{1,e}^{(n+1)}, q_{2,e}^{(0)}, \ldots, q_{2,e}^{(n+1)}, \ldots, q_{N_e,e}^{(n+1)}; q_{1,p}^{(0)}, \ldots, q_{N_p,p}^{(n+1)}\}$. Further details of the high-temperature path integral representation are given in [1, 2]. Figure 1 illustrates the representation of one (light) electron and one (heavy) proton. The circle around the electron beads symbolizes the region that mainly contributes to the partition function path integral. The size of this region is of the order of the electron thermal wavelength $\lambda_e(T)$, while typical distances between electron beads are of the order of the electron wavelength taken at ($n+1$)-times higher temperatures. The same representation is valid for proton. The spin gives rise to the spin part of the density matrix ($\mathcal{S}$) with exchange effects accounted for by the permutation operators $\hat{P}_e$ and $\hat{P}_p$ acting on the electron and proton coordinates $q^{(n+1)}$ and spin projections σ'. The sum in (2) is taken over all permutations with parities κ_{P_e} and κ_{P_p}. In the evaluation of the expressions obtained and their thermodynamic derivatives so far we make use of a Monte Carlo scheme [2]. Periodic boundary conditions are applied to the basic Monte Carlo cell.
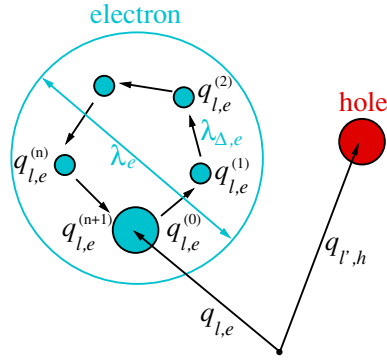
Figure 1. Bead representation of electron and proton (hole). Here $\lambda_e^2 = 2\pi\hbar^2\beta/m_e$, $\lambda_{\Delta,e}^2 = 2\pi\hbar^2\Delta\beta/m_e$, $q_{l,e}^{(1)} = q_{l,e}^{(0)} + \lambda_{\Delta,e}\xi_{l,e}^{(1)}$ and $\sigma = \sigma'$. The proton has a similar bead representation, however, λ_p and all length scales for it are $\sqrt{m_p/m_e}$ times smaller.
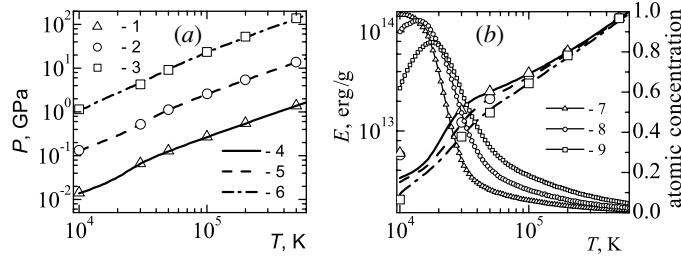

Figure 2. The DPIMC (1, 2, 3) and theoretical isochors (4, 5, 6) [3, 4] for pressure (a) and energy (b) in hydrogen plasma versus temperature; (7, 8, 9)—the relative number concentration of hydrogen atoms [3, 4].

3. Hydrogen plasma

3.1. Pressure and energy

In figure 2, the pressure and energy dependences versus temperature along three isochors of hydrogen plasma are shown. DPIMC calculations of isochors $n_e = 10^{20}, 10^{21}, 10^{22}$ cm^{-3} are presented by symbols 1, 2, 3, respectively. Analogous EOS calculations of isochors [3, 4] are given by lines 4, 5, 6 and relative number concentration of hydrogen atoms (on right axis of figure 2(b)) by lines with symbols 7, 8, 9. The agreement of DPIMC and EOS in chemical picture [3, 4] is very good for pressure and for energy at temperatures higher than 3×10^4 K. The relative number concentration of hydrogen atoms indicates that hydrogen at $T = 10^4$ K and $n_e = 10^{20}$–10^{22} cm^{-3} consists mainly of atoms.

In figure 3, the DPIMC results for pressure and internal energy of dense hydrogen are presented. This picture shows isotherms for the temperatures $10^4, 3 \times 10^4, 5 \times 10^4, 10^5$ K. It is well known that for ideal plasma the energy increases with density. The non-ideal hydrogen plasma, on the other hand, shows a significant deviation from this trend in a full agreement with the existing analytical predictions. Nevertheless, non-ideal plasma data asymptotically approach the standard results at low and high densities. At temperature $T = 10^4$ K, the ratio of the pressure to ideal plasma pressure approaches 0.5 indicating that electrons and protons form bound states (atoms). The formation of the pressure and energy minimum at intermediate
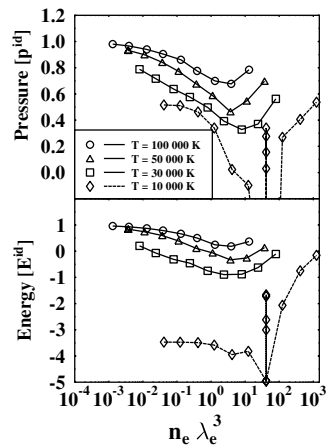
Figure 3. The DPIMC pressure and energy isotherms of dense hydrogen versus degeneracy parameter (λ_e is the electron thermal wavelength). For $T = 10^4$ K, in the range $10 \leqslant n_e\lambda_e^3 \leqslant 100$, due to many-particle clusters formation, strong fluctuations of the pressure and energy occur, so, as a consequence, the DPIMC simulation results do not converge (vertical lines).
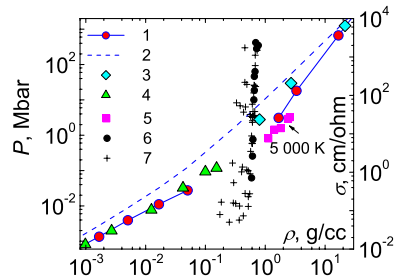

Figure 4. Pressure (1–5) (left axis) and electrical conductivity (6, 7) (right axis) for hydrogen at $T = 10^4$ K versus density. 1, DPIMC simulation; 2, ideal plasma; 3, DFT [5]; 4, restricted PIMC computations [6]. Experimental data: 5, break of the quasi-isentropic curve [7]; 6, electrical conductivity [8]; 7, electrical conductivity [9].

densities (around 10^{22} cm^{-3}) is due to the overall attractive Coulomb correlations leading in particular to the formation of atoms and molecules. At larger densities, the energy and pressure rapidly increase which is a consequence of electron degeneracy effects: increasing overlap of the electron wavefunctions leads to a break-up of bound states leading to the Mott effect and increase of the exchange energy. In the region of a possible plasma phase transition, the pressure in simulations becomes negative, indicating an instability of the homogenous plasma state. We observe large fluctuations of pressure and energy (shown by the vertical lines) related to the formation and decay of the many-particle clusters.

3.2. Hydrogen conductivity

Figure 4 presents EOS obtained by different authors for temperature $T = 10^4$ K and experimental data on conductivity obtained by Ternovoi *et al* and Weir *et al*. In figure 4, the diamonds (3) present data obtained by Hansen and Xu in the framework of the density functional theory (DFT) [5]. At low density they observe large fluctuations of pressure indicating the possible existence of a phase transition. Data obtained in the 'fixed node
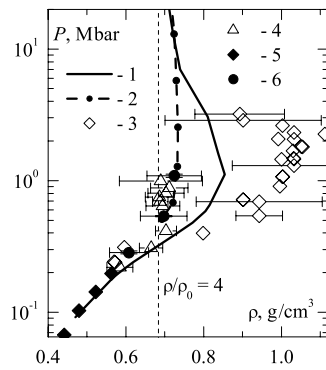
Figure 5. Shock Hugoniot of deuterium. 1, combined Hugoniot [12]; 2, RPIMC calculations [15]. Experimental data: 3, [14]; 4, [13]; 5, [11]; 6, [16].

approximation' [6] are presented by triangles (4). DPIMC calculations are presented by circles (1). Break on the isotherm is related to the negative values of the calculated pressure. On the left side of this break, homogeneous state of plasma becomes unstable giving rise to metallic-like many particle electron–proton clusters. On the right side of this break after the overlapping of these clusters, the plasma becomes uniform and stable again. The *position of the break* on the quasi-isentrope obtained in experiments by Mochalov [7] is shown by the squares (5); this break is supposed to be connected with a plasma phase transition. The overlap of many-particle clusters may result in sharp increase in conductivity (6, 7), which was observed experimentally [8, 9].

3.3. Deuterium Hugoniot

The high-pressure experimental results for the EOS are usually available in form of the shock Hugoniot. The Hugoniot equation relates the state behind the front of the shock-wave (namely, the density ρ, pressure P and specific internal energy E) to the initial conditions (ρ_0, p_0 and E_0). Figure 5 proposes a theoretical Hugoniot obtained by combining results for the EOS of the DPIMC technique and those of the reaction ensemble Monte Carlo (REMC) simulations performed in Rostock University. As shown by Bezkrovniy *et al* [10], REMC describes the low temperature region very well and shows a good agreement with the gas gun experiments by Nellis *et al* [11]. The DPIMC simulation has been performed at temperatures 10^4 K and higher in a wide range of particle densities. The influence of molecular states allowed us to calculate the Hugoniot reliably only above 8000 K. So we combined the lower part (up to 15 000 K) of the REMC Hugoniot and the DPIMC Hugoniot [12] (above 15 000 K). We want to stress here that these two methods are completely independent and no interpolation procedure is used. The final Hugoniot is plotted in figure 5 and shows a maximal compressibility of approximately 4.75 as compared to the initial normal condition deuterium density. This Hugoniot is located between the experimental values of Knudson *et al* [13] and Collins *et al* [14] and shows higher compressibility of deuterium at pressures about 1 Mbar than most of the other theories but lower values than [3].

4. Electron–hole plasma

Optical or electrical excitation of semiconductors allows us to create correlated electron–hole plasmas. Alternatively equilibrium electron–hole plasma can be created, for example,
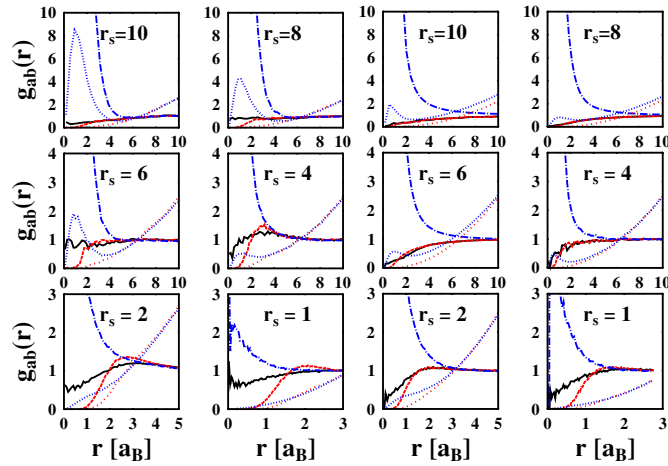
Figure 6. PDF for $T/E_b = 0.097$ (left two columns) and $T/E_b = 0.39$ (right two columns), respectively. The hole–electron mass ratio $M = m_h/m_e \simeq 40$ corresponds to conditions of [17].

by applying strong external pressure to the intermediate valent Tm[Se,Te] [17]. Electrons and holes can form such bound states as excitons (with binding energy E_b), bi-excitons, many-particle clusters. At high density, such plasma undergoes the Mott transition to the quasi-metallic electron–hole liquid.

4.1. Pair distribution functions

As an effect of the Coulomb and Fermi repulsion, the PDF g_{ee} (solid line) and g_{hh} (dashed line) vanish at small distances (figure 6). Here the plasma density is characterized by the Brueckner parameter r_s defined as ratio of the mean distance between all particles $d = \left(\frac{3}{4\pi(n_e+n_p)}\right)^{1/3}$ to the Bohr radius a_B, where n_e and n_h are electron and hole densities, respectively. The decay of the electron–electron correlations is essentially different from that of the hole–hole correlations due to the large mass difference. In the electron subsystem, quantum exchange and tunnelling are more pronounced and compete with the growth of Coulomb repulsion. The strong peak of g_{eh} (dotted-dashed line) is caused by excitons. This is confirmed by considering $r^2 g_{eh}(r)$ (dense dotted line), which is peaked around a_B. At the same time, g_{ee}, g_{hh} exhibit no peak structure, i.e. there is no indication for the bi-excitons, which is a consequence of high temperature and low density ($r^2 g_{hh}$ are presented by the rare dotted lines). The highest peak of $r^2 g_{eh}$ is observed for $r_s = 10$. For higher density (up to $r_s = 5$), it is decreased due to the ionization of the excitons and beginning of recombination into bi-excitons at $r_s = 6$ (see also [18]).

In the case of low temperature and high density ($r_s = 4 - 2$), the PDF g_{ee} and g_{hh} show distinct peaks close to $r = 3a_B$, pointing towards the formation of bi-excitons and many-particle clusters. Simulations revealed an instability of the homogeneous plasma state for densities around $r_s \sim 3$. This might be due to the formation of many-particle clusters. This instability gives strong indication for a transition from an insulator to a semi-metal phase experimentally observed in [17].

Finally, at still higher densities ($r_s = 1$), the many-particle clusters are fully destroyed due to the many-body effects (pressure ionization) and simulations reveal ordering of the holes into a liquid-like and even crystal-like structures [19].
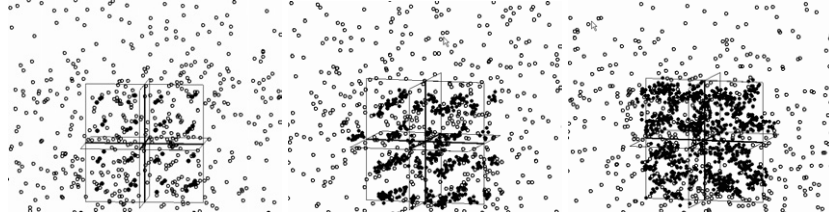
Figure 7. Electron–hole snapshots for $r_s = 0.5, M = 800, 100, 50$ (from left to right, respectively). Empty (filled) circles are electron (hole) beads.
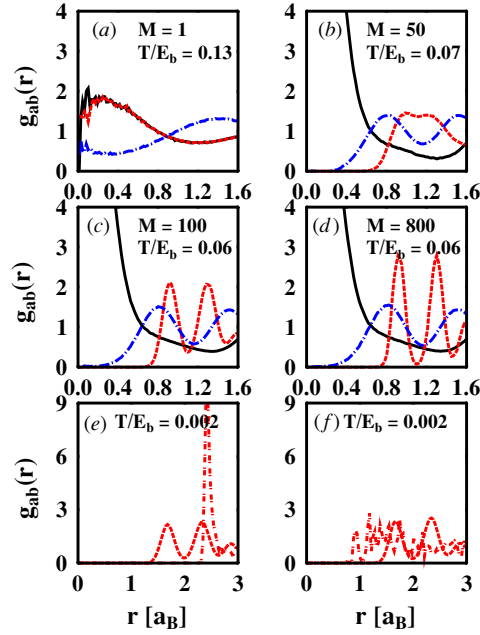

Figure 8. For quantum liquid-crystal hole transition, PDF g_{ab} averaged over spin projections are shown at $r_s = 0.5$ (a)–(d). Solid lines present g_{ee}, dashed lines—g_{hh}, dotted-dashed lines—g_{eh}. PDF g_{hh} for parallel (e) and antiparallel (f) spin projections relate to the transition of the hole crystal ($M = 400$—dashed lines) to the antiferromagnetic crystal structure ($M = 100$—dotted-dashed lines) with decreasing hole mass at $r_s = 0.9$.

5. Crystallization

Wigner (or Coulomb) crystallization appears to be a fundamental property common to all charged particle systems. It was observed experimentally in completely different systems, such as electrons on the surface of cold helium, ultra-cold ions in traps, in ion storage rings and so on. The necessary condition for the existence of a crystal is the mean Coulomb interaction energy to exceed the mean kinetic energy (thermal energy or Fermi energy). Coulomb crystallization of the holes and quantum melting were directly verified by the results presented in figure 7 showing snapshots of the electron–hole states in the simulation box at fixed temperature and density, but for decreasing values of $M = m_h/m_e$. In all figure parts, the electrons form a nearly homogeneous Fermi gas—the individual electrons penetrate each other and extend far beyond the main simulation cell (shown by the grid lines—to simulate a

macroscopic system, this cell is periodically repeated in three (X, Y, Z) space directions). At the same time, the hole arrangement changes dramatically. At $M = 800$, holes are periodically ordered in space, at $M = 100$ and between $M = 100$ and $M = 50$ the holes crystal is melting, at $M = 50$ the hole structure resembles liquid and at $M = 1$ the holes are in a gas-like state (similar to the electrons). The figure also clearly shows the mechanism of this quantum phase transition: with increase of M the individual hole wavefunctions shrink continuously until at $M = 800$ they collapse into a dot. The crystal melts when the decay length of the hole wavefunctions exceeds a critical size (around $M = 50$).

The quantum crystal-liquid transition at fixed temperature and density ($r_s = 0.5$) is further supported by the behaviour of the PDF, shown in figure 8(*a*)–(*d*). The figures show hole crystal formation with increasing hole mass. These simulations indicate also that the crystal phase is even more stable than predicted by the OCP plasma model in which the electrons are assumed to form a strictly uniform background. The physical reason for the hole-crystal stabilization can be understood from the behaviour of g_{ee} (figures 8(*b*)–(*d*)), which for ordered hole structures have the sharp peaks at small distances between electrons. So the density of the highly degenerated nearly free electrons in a hole periodic and quasi-periodic potential field is nonuniform and has interference maxima related to the variation of modulus of the electron wavefunctions. DPIMC calculations also show that quantum melting agrees with the Lindemann criterion.

Figures 8(*e*) and (*f*) demonstrate that at fixed density and very low temperature the electron–hole system with decreasing hole mass can form antiferromagnetic crystal-like structure consisting of two perfect hole lattices each containing the holes with the same spin projections. The physical reason of this phenomenon is the strong Fermi repulsion between particles with the same spin projection. Correlation between lattices is defined only by effective force repulsion, which is weaker at lower hole mass due to the tunnelling of the holes.

Acknowledgments

References

[1] Filinov V, Bonitz M and Fortov V 2000 *JETP Lett.* **72** 245
Filinov V, Bonitz M, Ebeling W and Fortov V 2001 *Plasma Phys. Control. Fusion* **43** 743
[2] Zamalin V, Norman G and Filinov V 1977 *The Monte Carlo Method in Statistical Thermodynamics* (Moscow: Nauka) (in Russian)
[3] Chabrier G, Saumon D, Hubbard W and Lunine J 1992 *Astrophys. J.* **391** 817–26
[4] Saumon D, Chabrier G and Van Horn H 1995 *Astrophys. J. Suppl. Ser.* **99** 713–41
[5] Xu H and Hansen J 1998 *Phys. Rev.* E **57** 211
[6] Militzer B and Ceperley D 2001 *Phys. Rev.* E **63** 066404
[7] Mochalov *et al* This volume
[8] Weir S, Mitchell A and Nellis W 1996 *Phys. Rev. Lett.* **76** 1860
[9] Ternovoi V Ya, Filimonov A S, Fortov V E, Kvitov S V, Nikolaev D N and Pyalling A A *et al* 1999 *Physica* B **265** 6
[10] Bezkrovniy V, Schlanges M, Kremp D and Kraeft W-D 2004 *Phys. Rev.* E **69** 061204
[11] Nellis W J, Mitchell A C, van Thiel M, Devine G J, Trainor R J and Brown N 1983 *J. Chem. Phys.* **79** 1480

[12] Bezkrovniy V, Filinov V, Kremp D, Bonitz M, Schlanges M, Kraeft W-D, Levashov P and Fortov V 2004 *Phys. Rev.* E **70** 057401
[13] Knudson M D, Hanson D L, Bailey J E, Hall C A, Asay J R and Deeney C 2004 *Phys. Rev.* B **69** 144209
[14] Collins G, Da Silva L, Celliers P, Gold D, Foord M, Wallace R, Ng A, Weber S, Budil K and Cauble R 1998 *Science* **281** 1178
[15] Militzer B and Ceperley D M 2000 *Phys. Rev. Lett.* **85** 1890
[16] Boriskov G V, Bykov A I, Il'kaev R I, Selemir V D, Simakov G V, Trunin R F, Urlin V D, Shuikin A N and Nellis W J 2005 *Phys. Rev.* B **71** 092104
[17] Neuenschwander J and Wachter P 1990 *Phys. Rev.* B **41** 12693
[18] Fehske H, Filinov V S, Bonitz M, Levashov P and Fortov V E 2005 *J. Phys.: Conf. Ser.* **11** 139
[19] Bonitz M, Filinov V S, Fortov V E, Levashov P and Fehske H 2005 *Phys. Rev. Lett.* submitted (see also paper in this volume)